High-order nonlinear dipole response characterized by extreme ultraviolet ellipsometry

KUANG-YU CHANG,[1] LONG-CHENG HUANG,[1] KOJI ASAGA,[2,3] MING-SHIAN TSAI,[1] LAURA REGO,[4] PEI-CHI HUANG,[1] HIROKI MASHIKO,[2] KATSUYA OGURI,[2] CARLOS HERNÁNDEZ-GARCÍA,[4] MING-CHANG CHEN[1,5,6,*]

[1]*Institute of Photonics Technologies, National Tsing Hua University, Hsinchu, Taiwan*
[2]*NTT Basic Research Laboratories, 3-1 Morinosato Wakamiya, Atsugi, Kanagawa 243-0198, Japan*
[3]*Department of Electronic Engineering, Tokyo Denki University, 5 Senju-Asahi-cho, Adachi-ku, Tokyo 120-8551, Japan*
[4]*Grupo de Investigación en Aplicaciones del Láser y Fotónica, Departamento de Física Aplicada, University of Salamanca, Salamanca, Spain*
[5]*Department of Physics, National Tsing Hua University, Hsinchu, Taiwan*
[6]*Frontier Research Center on Fundamental and Applied Sciences of Matters, National Tsing Hua University, Hsinchu, Taiwan*
**Corresponding author: mingchang@mx.nthu.edu.tw*

S1. Energy-resolved EUV polarimeter

We report what we believe to be the first all-optical energy-resolved EUV polarimeter, which differs from previously published results [1,2] in which only monochromatic light could be measured. Adding one diffraction element and recording all spectral responses (see Fig. S1) allows us to resolve all polarization information of the broadband harmonics from HHG. It takes ≅ 1 min to complete one polarization characterization of all harmonic orders.

The Stokes vector that describes the complete polarization state of the electromagnetic wave has four parameters as

$$S = \begin{bmatrix} S_0 \\ S_1 \\ S_2 \\ S_3 \end{bmatrix} = \begin{bmatrix} I \\ I_p cos2\phi cos2\chi \\ I_p sin2\phi cos2\chi \\ I_p sin2\chi \end{bmatrix} \quad (1)$$

in which S_0, S_1, S_2, S_3 are the four Stokes parameters, I is total intensity of the beam, I_p, ϕ and χ are spherical coordinates of the three-dimensional vectors. When the beam is reflected by a polarization-altering component such as the gold mirrors in our polarimeter, the additional phase shift and amplitude reflectance between s- and p-polarizations that come from this component can be represented with a Mueller matrix, which is expressed as

$$M(\gamma, \Delta) = \begin{bmatrix} 1 & \cos2\gamma & 0 & 0 \\ \cos2\gamma & 1 & 0 & 0 \\ 0 & 0 & sin2\gamma cos\Delta & -sin2\gamma sin\Delta \\ 0 & 0 & sin2\gamma sin\Delta & sin2\gamma cos\Delta \end{bmatrix} \quad (2)$$

$$tan\gamma = \frac{r_p}{r_s} \quad (3)$$

$$\Delta = \delta_p - \delta_s \quad (4)$$

in which Mueller matrix M is defined to transform the incident Stokes vector into the exiting Stokes vector, r_p and r_s are the amplitude reflectances for p- and s-polarizations, and δ_p and δ_s are the phase shifts for p- and s-polarizations. Moreover, each chamber rotates through its angle during the measurement, so the rotation matrix is applied for the variation of the original coordinates of the incident measured light source.

$$R(\theta) = \begin{bmatrix} 1 & 0 & 0 & 0 \\ 0 & cos2\theta & sin2\theta & 0 \\ 0 & -sin2\theta & cos2\theta & 0 \\ 0 & 0 & 0 & 1 \end{bmatrix} \quad (5)$$

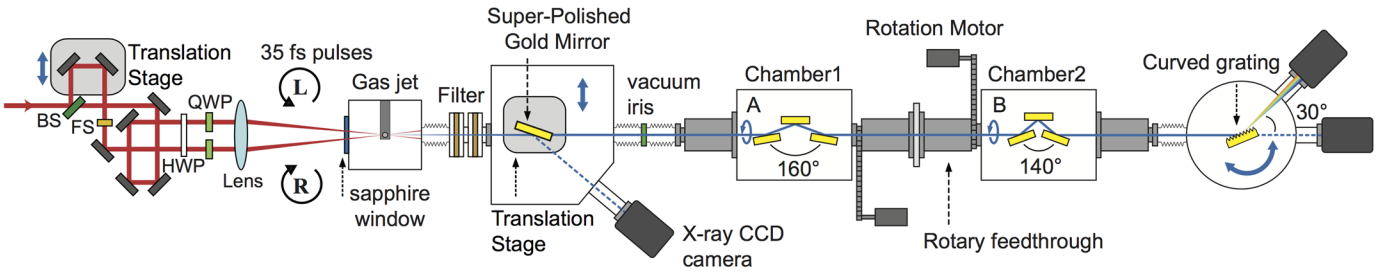

Fig. S1: Ellipticity-tunable HHG and energy-resolved EUV polarimeter. Top view of the experimental setup of the polarimeter in the HH ellipsometry study. BS: beam splitter, FS: fused silica for dispersion compensator, HWP: half-wave plate, QWP: quarter-wave plate.

After passing through two chambers and one curved grating, the Stokes vector of the output light field is expressed as

$$S_{out} = K \times M(\gamma_3)R(-B)M(\gamma_2,\Delta_2)R(B)R(-A)M(\gamma_1,\Delta_1)R(A)S_{in} \quad (6)$$

in which A and B are the rotation angles of two mirror sets. After applying the Mueller and rotation matrices and expanding all matrix chains, the output intensity is obtained as

$$\begin{aligned} S_{out} = S_0 &= K \times F(S_1/S_0, S_2/S_0, S_3/S_0, \gamma_1, \gamma_2, \gamma_3, \Delta_1, \Delta_2; A, B) \\ &= K \\ &+ cos2\gamma_3\{(cos2B\ sin2B \\ &- cos2B\ sin2B\ sin2\gamma_2\ cos\Delta_2) \\ &\times [S_1/S_0\ (cos2A\ sin2A - cos2A\ sin2A\ sin2\gamma_1\ cos\Delta_1) \\ &+ Ksin2A\ cos2\gamma_1 + S_2/S_0\ [(sin2A)^2 + (cos2A)^2\ sin2\gamma_1\ cos\Delta_1] \\ &- S_3/S_0\ cos2A\ sin2\gamma_1\ sin\Delta_1] \\ &+ [(cos2B)^2 + (sin2B)^2\ sin2\gamma_2\ cos\Delta_2] \\ &\times [Kcos2A\ cos2\gamma_1 \\ &+ S_2/S_0\ [cos2A\ sin2A - cos2A\ sin2A\ sin2\gamma_1\ cos\Delta_1] \\ &+ S_1/S_0\ [(cos2A)^2 + (sin2A)^2\ sin2\gamma_1\ cos\Delta_1] \\ &+ S_3/S_0\ sin2A\ sin2\gamma_1\ sin\Delta_1] \\ &+ cos2B\ cos2\gamma_2[K + S_1/S_0\ cos2A\ cos2\gamma_1 \\ &+ S_2/S_0\ sin2A\ \ cos2\gamma_1] \\ &+ sin2B\ sin2\gamma_2\ sin\Delta_2[S_3/S_0\ sin2\gamma_1\ cos\Delta_1 \\ &+ S_2/S_0 cos2A\ sin2\gamma_1\ sin\Delta_1 - S_1/S_0\ \ sin2A\ sin2\gamma_1\ sin\Delta_1]\} \\ &+ cos2B\ cos2\gamma_2\{Kcos2A\ cos2\gamma_1 \\ &+ S_2/S_0\ \ (cos2A\ sin2A - cos2A\ sin2A\ sin2\gamma_1\ cos\Delta_1) \\ &+ S_1/S_0\ [(cos2A)^2 + (sin2A)^2\ sin2\gamma_1\ cos\Delta_1] \\ &+ S_3/S_0\ \ sin2A\ sin2\gamma_1\ cos\Delta_1\} \\ &+ sin2B\ cos2\gamma_2\{S_1/S_0\ (cos2A\ sin2A \\ &- cos2A\ sin2A\ sin2\gamma_1\ cos\Delta_1) + Ksin2A\ cos2\gamma_1 \\ &+ S_2/S_0\ [(sin2A)^2 + (cos2A)^2\ sin2\gamma_1\ cos\Delta_1] \\ &- S_3/S_0\ \ cos2A\ sin2\gamma_1\ sin\Delta_1\} + S_1/S_0\ \ cos2A\ cos2\gamma_1 \\ &+ S_2/S_0\ \ sin2A\ cos2\gamma_1 \end{aligned} \quad (7)$$

in which K is a constant parameter of the system. As there are nine unknowns — $K, S_1/S_0, S_2/S_0, S_3/S_0, \gamma_1, \gamma_2, \gamma_3, \Delta_1, \Delta_2$, their solution requires at least nine equations, which are created on rotation angles A and B of the two chambers as shown in Fig. S1. In our experiments, we implemented over-sampling on taking a 16-$[A, B]$-angle combination of $[0, 0]$, $[0, \pi/4]$, $[0, \pi/2]$, $[0, 3\pi/4]$, $[\pi/4, 0]$, $[\pi/4, \pi/4]$, $[\pi/4, \pi/2]$, $[\pi/4,3\pi/4]$, $[\pi/2, 0]$, $[\pi/2, \pi/4]$, $[\pi/2, \pi/2]$, $[\pi/2,3\pi/4]$, $[3\pi/4, 0]$, $[3\pi/4, \pi/4]$, $[3\pi/4, \pi/2]$ and $[3\pi/4,3\pi/4]$ with respect to the horizontal plane of the optical breadboard. We then applied these 16 intensities to a genetic algorithm to minimize the deviation of those 16 observations from the theoretical values using Eq. (7). Last, the retrieved Stokes parameters (S_1, S_2, S_3) determined ellipticity ε, helicity, tilt angle τ, and degree of polarization p as

$$\varepsilon = tan\left[\frac{1}{2}atan\left(\frac{S_3}{\sqrt{{S_1}^2 + {S_2}^2}}\right)\right] \quad (8)$$

$$helicity = sign(\varepsilon) \quad (9)$$

$$\tau = atan(S_2/S_1)/2 \quad (10)$$

$$p = \frac{\sqrt{{S_1}^2 + {S_2}^2 + {S_3}^2}}{S_0} \quad (11)$$

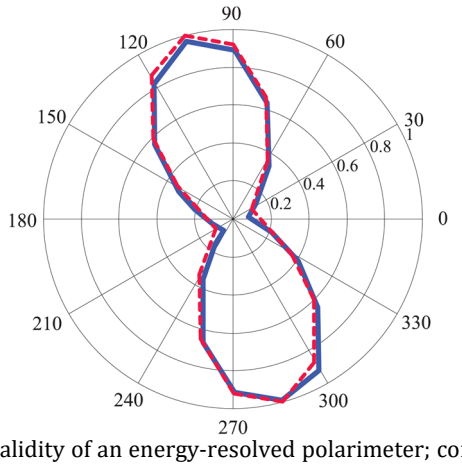

Fig. S2: Validity of an energy-resolved polarimeter; comparison of two EUV transmission curves vs. rotation angle of two rotating chambers proves the validity of the polarimeter. The blue line is the recorded transmission of harmonic 21 at the rotation condition $A = B$ with increasing step 15°. The red dashed line is generated from the Mueller matrix calculation based on parameters retrieved from another individual experiment. Further details are given in the text.

The amplitude ratio and phase shift between p- and s-polarizations for the first and the second rotation sets, together with the amplitude ratio induced by the grating can be solved simultaneously (i.e., γ_1 and Δ_1, γ_2 and Δ_2, and γ_3).

To confirm the validity of the novel energy-resolved polarimeter, we undertook a comparison on performing two individual experiments. The first experiment was to record the transmission of one specific harmonic in a particular rotation sequence of A and B. In this example, we sampled 24 points of the transmission of harmonic order 21 on rotating two chambers incrementally at the condition $A = B$ in 360°. The blue line in Fig. S2 presents the EUV transmission as a function of rotation angle A (or B). The second experiment was performed to measure the transmission at harmonic order 21 at the 16-$[A, B]$-angle combination of $[0, 0]$, $[0, \pi/4]$, $[0, \pi/2]$, $[0, 3\pi/4]$, $[\pi/4, 0]$, $[\pi/4, \pi/4]$, $[\pi/4, \pi/2]$, $[\pi/4,3\pi/4]$, $[\pi/2, 0]$, $[\pi/2, \pi/4]$, $[\pi/2, \pi/2]$, $[\pi/2,3\pi/4]$, $[3\pi/4, 0]$, $[3\pi/4, \pi/4]$, $[3\pi/4, \pi/2]$ and $[3\pi/4,3\pi/4]$. Then listing these 16 equations based on Eq. (7), we solved and retrieved the polarization state of harmonic order 21, while also obtaining all other unknown parameters of the

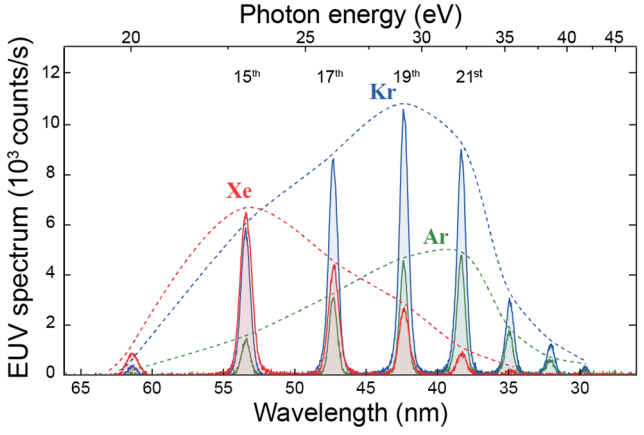

Fig. S3: Spectra of elliptically polarized HHG. Harmonic emissions from non-collinear geometry in Ar, Kr and Xe driven by crossing two 35-fs 800-nm pulses.

Table S1. Parameters of the driving IR fields used in this HH ellipsometry work

Gas	Pulse energy of each IR beam (μJ)	Ellipticity of two counter-rotating IR ε_{IR}	Peak intensity on the focal plane (10^{14} W/cm^2)		Average peak intensity $(I_{IR.s}+I_{IR.p})/2$ (10^{14} W/cm^2)	Peak intensity difference $\Delta I_{IR}=I_{IR.s}-I_{IR.p}$ (10^{14} W/cm^2)
			$I_{IR.s}$	$I_{IR.p}$		
Ar	130	0.9	3.11	2.52	2.82	0.59
		0.8	3.43	2.20		1.24
		0.7	3.79	1.85		1.93
Kr	120	0.9	2.87	2.33	2.6	0.55
		0.85	3.02	2.18		0.84
		0.8	3.17	2.03		1.14
Xe	100	0.95	2.27	2.04	2.16	0.22
		0.9	2.39	1.93		0.45
		0.85	2.51	1.81		0.70

amplitude ratio and the phase shift from two rotation sets, and the amplitude ratio of the EUV grating between p- and s-polarizations. Based on those retrieved parameters, the red dashed curve in Fig. S2 was generated from the Mueller matrix calculation (Eq. (6)), according to the angle sequence of the first experiment, in which $A = B$. The two curves match satisfactorily in the polar diagram, directly proving the validity of the energy-resolved EUV polarimeter implemented in this study.

S2. Driving laser fields vs. HH polarization in Ar, Kr and Xe

Two elliptically polarized fundamental beams with the same ellipticity and tilt angle but opposite helicity were focused into a gas jet non-collinearly as shown in Fig. S1. In this work, the pulse energy of the two IR arms was carefully tuned to be identical, being 130, 120, 100 μJ for HHG in Ar, Kr, Xe, respectively. The average peak intensity of the crossing beam on the focal plane was estimated to be 2.82×10^{14}, 2.6×10^{14}, 2.16×10^{14} W/cm^2 in Ar, Kr, Xe as listed in Table S1. Fig. S3 shows one of their harmonic spectra. Fig. S4 presents polarization scaling of HH pulses in Ar, Kr and Xe vs. ε_{IR}.

S3. Beam divergence of elliptically polarized HH

Fig. S5 shows the beam profiles of EUV beams driven by IR with ellipticity $\varepsilon_{IR} = 0.9$ and 0.8 in Ar, Kr and Xe. It is clear that high-order diffraction patterns appear when a small ellipticity of driving pulses is applied. As slightly elliptically polarized IR light made a stronger high-harmonic dipole modulation in both intensity and phase, as one grating in the focal plane through

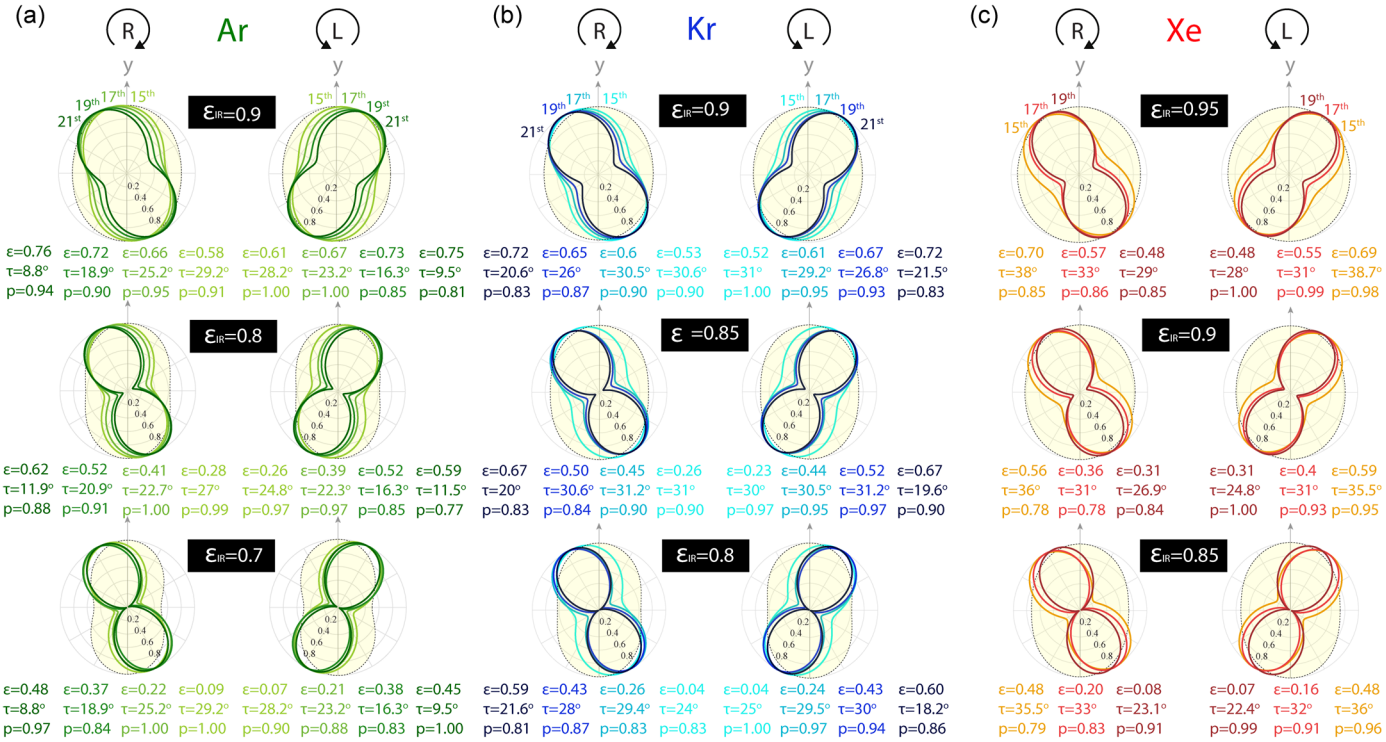

Fig. S4: Polarization scaling of HH pulses in Ar, Kr and Xe. The polarization states of the input IR (yellow area with black dashes) and output HHG EUV (green lines for Ar, blue for Kr and red for Xe) were measured with the IR polarization analyzer and the energy-resolved EUV polarimeter, respectively, and are depicted in the polar plots, with a table indicating the observed ellipticity ε, tilt angle τ and degree of polarization p varying with ε_{IR}. The color gradient presents the various harmonic orders q.

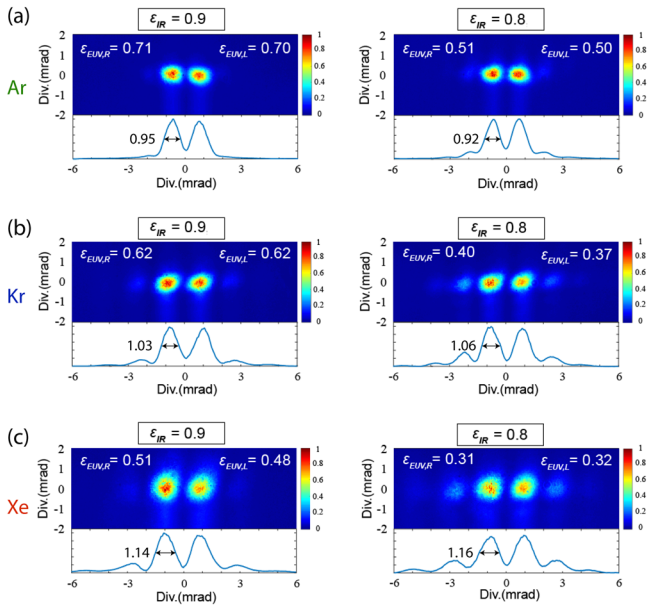

Fig. S5: Far-field HH beam profile. The beam profiles of left- and right- handed elliptically polarized high harmonic pulses driven by IR with $\varepsilon_{IR} = 0.9$ and 0.8 in (a) Ar, (b) Kr and (c) Xe.

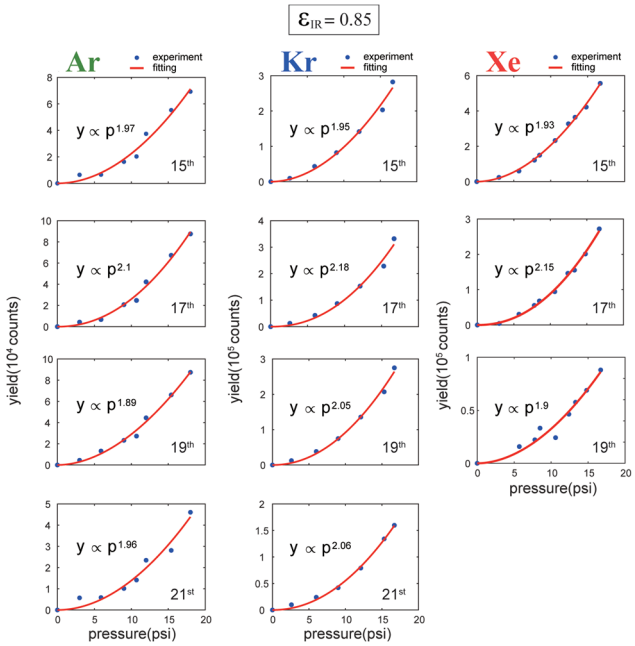

Fig. S6: Quadratic HHG yield growth vs. pressure. The dots represent the experimental pressure-tuned HHG yield as a function of pressure, when driven by IR with $\varepsilon_{IR} = 0.85$ in the non-collinear geometry. Red curves are made for a power scale fit using $y = c \times p^{\gamma}$, in which y is the observed HH yield, c is a parameter and γ is the pressure-dependent power factor.

the transverse direction. Especially for Xe, even the third-order diffraction was clearly observed when HH radiation was driven with $\varepsilon_{IR} = 0.8$. The reason is that both amplitude and phase of high-harmonic dipole scale vary more rapidly with the driving field in a gas of smaller ionization potential. In Ar, the intensity of the first-order diffraction of HH contained 91 % of the total harmonic yield when driven with $\varepsilon_{IR} = 0.9$, whereas the energy ratio of the first order dropped to 83 % when driven with $\varepsilon_{IR} = 0.8$. In Kr (Xe), the energy ratio decreased from 83 % (80 %) to 73 % (70 %) using $\varepsilon_{IR} = 0.9$ and $\varepsilon_{IR} = 0.8$, respectively. In contrast, the resulting EUV radiation became more linearly polarized. On comparing these results, the EUV ellipticity in Xe was always the least.

About the beam profiles of the first diffraction order, the divergence of the emitted harmonics varied little with IR ellipticity ε_{IR}. We refer the reader's attention to the divergence comparison of HH in varied gaseous species. The divergence of HH radiation was observed to increase in the order Ar, Kr, Xe. This observation also shows a satisfactory agreement with the conclusion from the main text. Because both q_{eff} and α are larger for Xe (Fig. 3 in the main text), a Gaussian profile of the fundamental would produce the HH emission of smaller size, together with a larger wavefront divergence (a larger phase advance shift) in Xe among them.

S4. Macroscopic IR propagating effect in non-collinear HHG

In the focal plane, the interference of two fundamentals leads to local E-field vectors that rotate across direction x. In such a configuration, $E_{IR.y}$ is always stronger than $E_{IR.x}$ if ε_{IR}<1 (one example is given in Fig. S8). In the focal plane, at the location at which $E_{IR.y}$ dominated, the local intensity increased. Two possible nonlinear effects might induce an additional phase shift between $E_{IR.y}$ and $E_{IR.x}$: i) plasma-induced change of refraction index and ii) self-phase modulation (SPM). To verify whether the IR propagating effects played a crucial role in polarization control of HHG, we performed two pressure-dependent experiments driven by IR pulses with $\varepsilon_{IR} = E_{IR.x}/E_{IR.y} = 0.85$. The reason is that the change of refraction index induced by

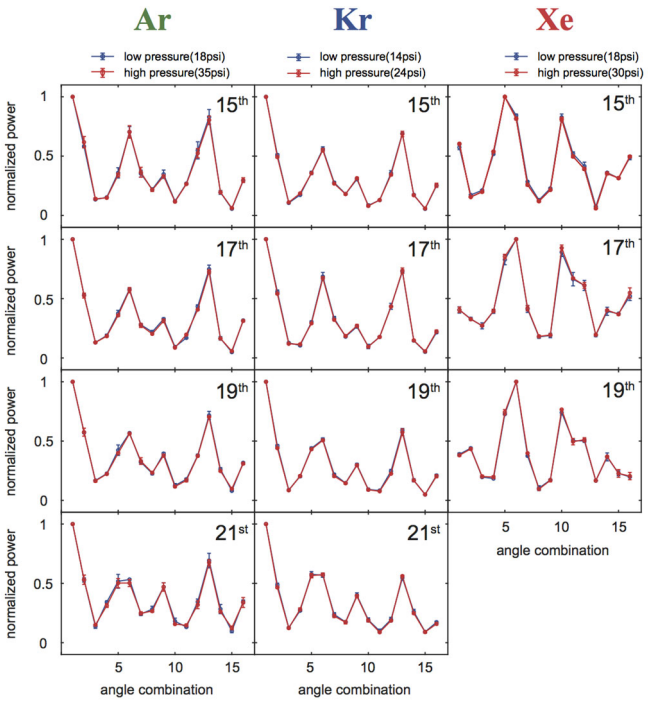

Fig. S7: Polarization state vs. pressure. Blue (red) curves show the measured transmissions after an all-optical polarimeter in the 16-$[A, B]$-angle combination under a HHG backing pressure of ≈18 psi (≈30 psi). As mentioned in Section S1, those 16-$[A, B]$-angle combinations are $[0, 0]$, $[0, \pi/4]$, $[0, \pi/2]$, $[0, 3\pi/4]$, $[\pi/4, 0]$, $[\pi/4, \pi/4]$, $[\pi/4, \pi/2]$, $[\pi/4, 3\pi/4]$, $[\pi/2, 0]$, $[\pi/2, \pi/4]$, $[\pi/2, \pi/2]$, $[\pi/2, 3\pi/4]$, $[3\pi/4, 0]$, $[3\pi/4, \pi/4]$, $[3\pi/4, \pi/2]$ and $[3\pi/4, 3\pi/4]$. The transmission powers of HHG under low and high pressures were normalized to their maxima respectively. Error bars are derived from five individual measurements.

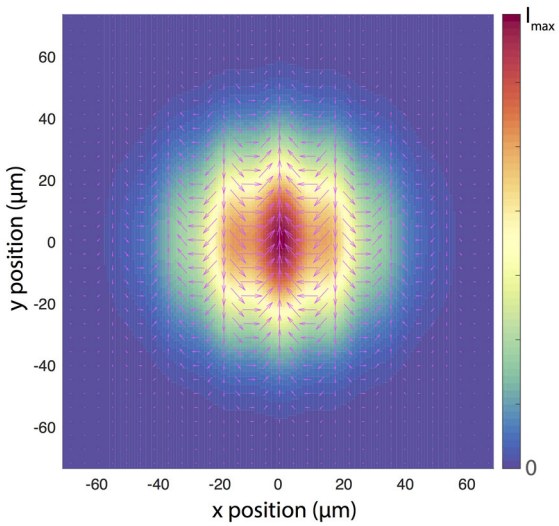

Fig. S8: Calculated snapshot of the driving IR vectors in the focal plane. *E*-field vectors on focusing two identical elliptically polarized IR beams with equal ellipticity and intensity but opposite helicity. Based on experimental parameters, the IR focus is a Gaussian distribution with waist ω_0 = 40 μm. The half-crossing angle between the two non-collinear IR beams is 20.9 mrad. I_{max} represents the peak intensity of the focus. In this calculation, ε_{IR} is 0.9.

those two nonlinear effects is proportional to the backing pressure. The first experiment was to measure the HH yield as a function of backing pressure, as shown in Fig. S6. It clearly presents that every order of HHG in Ar, Kr and Xe exhibits a quadratic dependence on pressure, indicating that the plasma has no influence on propagation of the fundamental beams.

The second experiment consisted of identifying whether the resulting polarization state varied with pressure. Fig. S7 clearly shows that the resulting polarization state of HHG was not associated with the backing pressure. We observed that, under backing pressures 18 and 30 psi, the resulting HH beams had almost identical polarizations, as recorded by the 16-[A, B]-angle combination.

According to those two experiments, we concluded that the polarization control results presented in this work can not be attributed to an IR propagation effect.

S5. Retrieval of single-atom scaling parameters in amplitude and phase (q_{eff} and α) from the far-field polarimeter observations (ε_{EUV} and τ)

IR laser amplitude E_0, half-crossing angle ξ and ellipticity ε_{IR} were well calibrated experimentally for the retrieved input. With two identical elliptically polarized IR beams focused with equal ellipticity and intensity but opposite helicity, Fig. S8 plots one example of the calculated IR vectors in the focal plane.

Each local linearly polarized IR field produced linearly polarized HH emission in the near field based on the dipole response of harmonic order q as a function of the laser field as

$$E_{EUV}(I_{IR}) \propto A_q(I_{IR}) \exp[i\theta_q(I_{IR})] \cong I_{IR}^{q_{eff}/2} \exp[-iI_{IR}\alpha] \quad (12)$$

in which q_{eff} is an effective order of nonlinearity, and $\theta_q(I_{IR}) \cong -I_{IR}\alpha$ is the phase of harmonic order q [3-5] , while the vector direction of E_{EUV} follows that of E_{IR}.

The far-field response was obtained on considering an infinitely thin medium and summing the contributions of all atomic emissions located in the plane of generation based on Eq. (12), following the Huygens–Fresnel principle. The state of polarization of HHG in the far field is a coherent sum of Eqs. (1) and (2) in the main text for *p*- and *s*-polarizations, resulting in two main diffraction EUV beams in the direction of ξ/q, from which we calculated ellipticity $\varepsilon_{EUV.cal}(q_{eff},\alpha)$ and tilt angle $\tau_{cal}(q_{eff},\alpha)$.

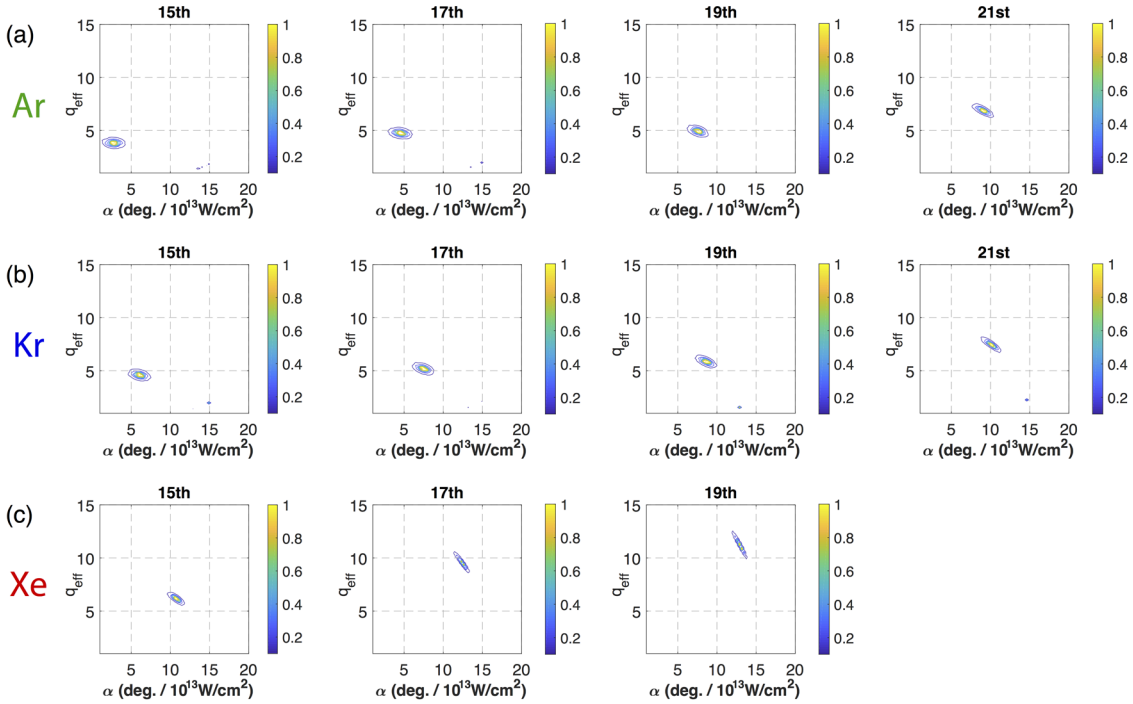

Fig. S9: Retrieval of q_{eff} and α from ε_{EUV} and τ; normalized two-dimensional fitness function as a function of q_{eff} and α that meets the polarimeter observation of ε_{EUV} and τ driven with two IR beams with $\varepsilon_{IR} = 0.9$ in (a) Ar, (b) Kr, and (c) Xe.

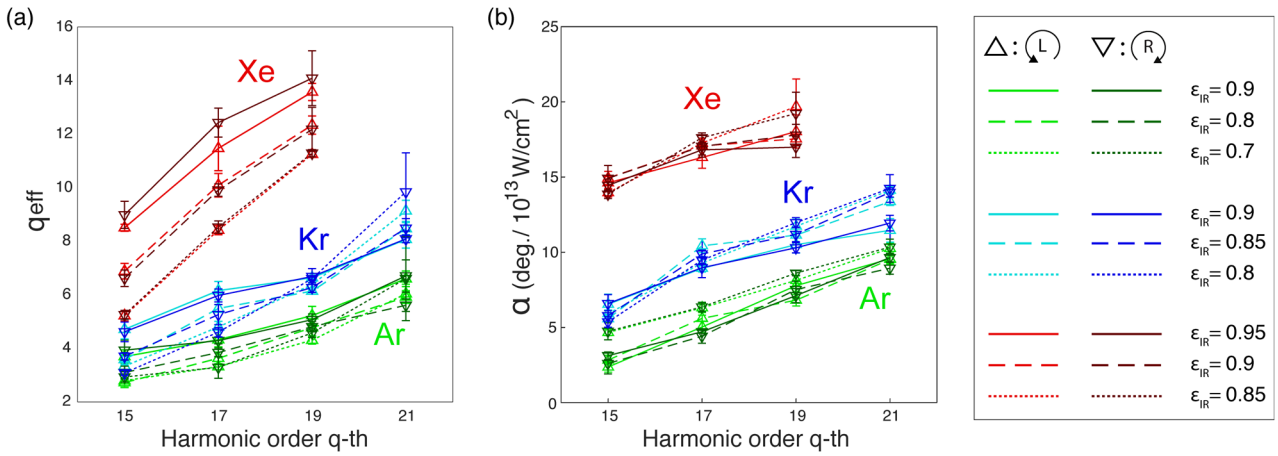

Fig. S10: Extracted dipole response information from HH ellipsometry. (a) retrieved power scaling q_{eff} vs. harmonic order q. (b) phase-intensity slope α vs. harmonic order q based on all observed ε_{EUV} and τ driven with varied ε_{IR} (Fig. S4 and Fig. 2 in the main text). The standard deviations are derived from five individual measurements.

We defined a fitness function that describes the sum of deviations in ε_{EUV} and τ between theoretical calculation and experimental polarization measurement as

$$Fitness(q_{eff},\alpha)= \frac{1}{c_1\left[\frac{\varepsilon_{EUV.cal}(q_{eff},\alpha)-\varepsilon_{EUV.exp}}{1}\right]^2+\left[\frac{\tau_{cal}(q_{eff},\alpha)-\tau_{exp}}{180}\right]^2}, \quad (13)$$

in which $\varepsilon_{EUV.exp}$ and τ_{exp} are the observed experimental EUV ellipticity and tilt angle. While considering different units in ε_{EUV} and τ, the two deviations are normalized by their maximum values $\varepsilon_{EUV}=1$ and $\tau=180^{o}$, respectively. Parameter c_1 is a weighting factor between those two deviations. Fig. S9 uses c_1=1. By directly calculating two-dimensional $Fitness(q_{eff},\alpha)$ and seeking the maximum value and its index location of q_{eff} and α, we observed one robust main peak in the range q_{eff} from 0 to 15, and α from 1 to 20 (Deg./(10^{13} W/cm^2)). Note that a change of weighting factor c_1 barely alters the peak locations. Their peak values are of order $\approx 10^9$ (deviations $\approx 10^{-9}$), indicating stable and excellent fitting results.

Fig, S10 presents all retrieved single-atom scaling parameters in amplitude and phase, q_{eff} and α, based on observations of ε_{EUV} and τ (Fig. S4 and Fig. 2 in the main text) driven by varied ε_{IR} and intensities (Table S1) in three gases. The statistics of all retrieved q_{eff} and α are presented in Fig. 3 in the main text.

Based on those retrieved q_{eff} and α, the amplitude ratio ($E_{EUV.p}/E_{EUV.s}$) and the phase shift ($\theta_{EUV.p}-\theta_{EUV.s}$) induced by the peak of two perpendicular fundamentals, $E_{IR.s}$ and $E_{IR.p}$ (located at two separate positions marked in the main text Fig.

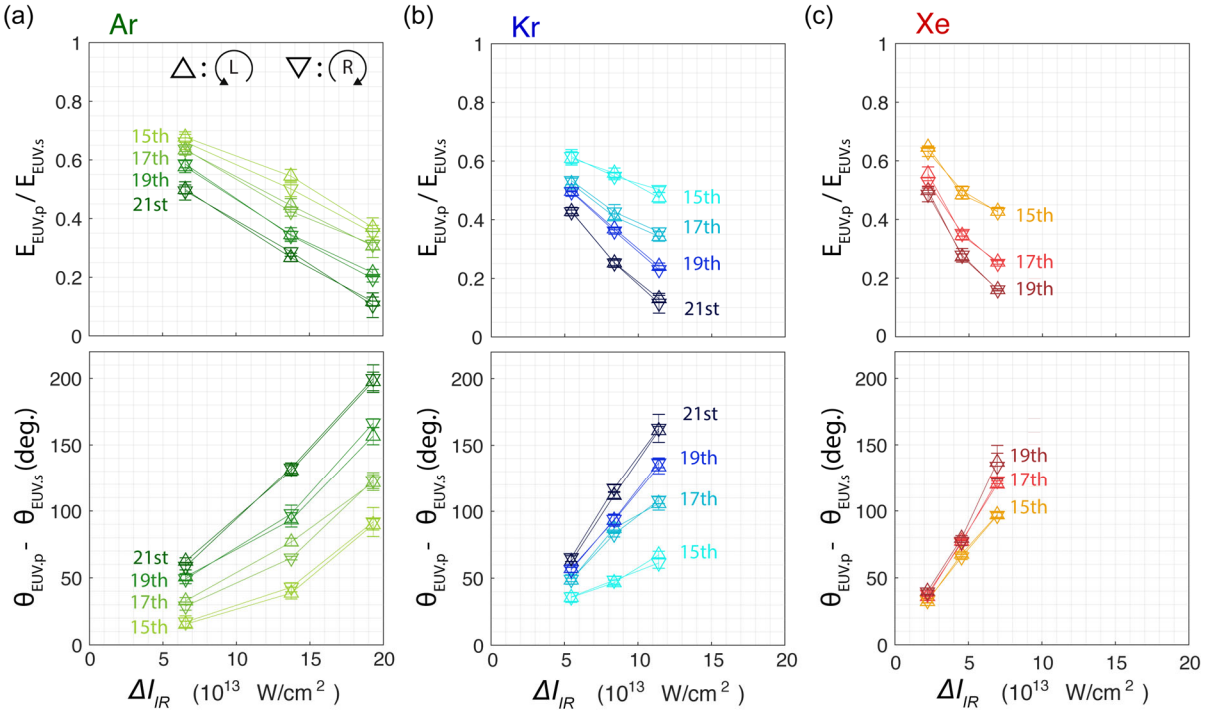

Fig. S11. Retrieved $E_{EUV.p}/E_{EUV.s}$ and $\theta_{EUV.p}-\theta_{EUV.s}$ between two positions marked in magenta in the main text Fig. 1(a) in which the dipole is driven by peaks of their two perpendicular fundamentals. Based on Fig. S10, retrieved amplitude ratio $E_{EUV.p}/E_{EUV.s}$ and retrieved atomic phase difference $\theta_{EUV.p}-\theta_{EUV.s}$ vs. their intensity variations, $\Delta I_{IR}=I_{IR.s}-I_{IR.p}$ in (a) Ar, (b) Kr and (c) Xe.

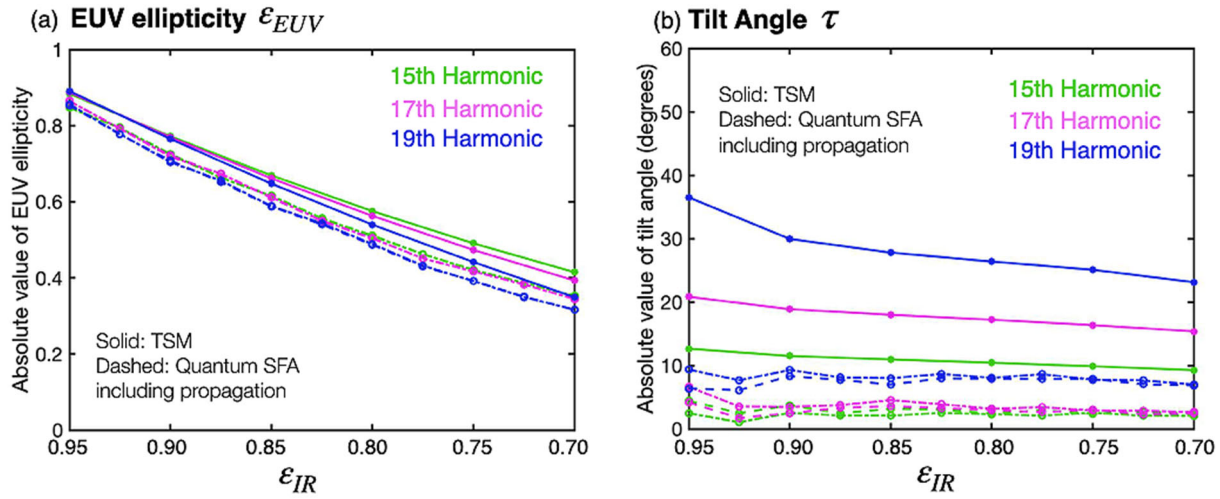

Fig. S12: Simulation results of EUV ellipticity and tilt angle in Ar. (a) EUV ellipticity ε_{EUV} and (b) tilt angle τ as a function of IR ellipticity ε_{IR} calculated through the SFA quantum (dashed line for the right-handed helicity, dotted-dashed line for the left-handed helicity) and TSM (solid lines), for harmonics 15 (green), 17 (pink) and 19 (blue).

1(b)) were calculated vs. their intensity difference $\Delta I_{IR} = I_{IR.s} - I_{IR.p}$, as presented in Fig. S11.

S6. Ellipticity and tilt-angle results from theoretical simulations

To validate the dipole phase (α) and power scaling (q_{eff}) coefficients retrieved from experimental HH ellipsometry, we present in this section theoretical simulations from two distinct and complementary models.

I) First, we used the thin-slab model (TSM) [6,7]. In this simplified description, the target is represented by a thin (2D) slab placed at the transverse focal plane, where the high-order harmonics are emitted. From the strong-field description, we consider that the harmonic amplitude corresponds to power q_{eff} of the fundamental amplitude; the harmonic phase presents an additional non-perturbative phase, the so-called dipole phase, which is proportional to the intensity of the fundamental field through strong-field parameter α^j, which depends on quantum path *j* followed by the electronic wave packet in the HHG process. To calculate the harmonic emission in the far field we used Fraunhofer diffraction. A complete description of this model can be found in Refs. [6,7]. Remarkably, this TSM has been used to reproduce the polarization control of high-order harmonics in a non-collinear geometry [8].

II) Second, we performed quantum strong-field approximation (SFA) calculations including propagation through the electromagnetic field propagator [9]. The dipole acceleration at each atom in the target is calculated through the quantum strong-field approximation (SFA) [10-12], without resorting in the saddle-point approximation. The macroscopic far-field harmonic emission is computed as the coherent addition of that of each elementary radiator at the target. The high-order harmonic radiation is assumed to propagate towards the far field with a phase velocity equal to the speed of light. Propagation effects of the fundamental field are taken into account. This method has been already used to reproduce the polarization control in the non-collinear HHG geometry [8,13,14].

In Fig. S12 we present the theoretical results in Ar obtained from the TSM and the quantum SFA simulations for (a) EUV ellipticity ε_{EUV} and (b) tilt angle τ, using parameters similar to those in the experiment. We implemented each non-collinear driver as a Gaussian beam of waist 34 μm, with half-crossing angle $\xi = 21.65$ mrad, wavelength 800 nm and field amplitude $E_0 = 0.063$ atomic units, as defined in Eqs. (3) and (4) of the main text. In the quantum SFA simulations, we modeled the laser pulse with a $\sin^2$ envelope of pulse duration 11.5 fs full-width at half maximum intensity. In the TSM calculations we chose field amplitude 0.057 a. u., corresponding to an intensity 80 % of that of the SFA calculations, which showed superior agreement with the experimental results. The strong-field parameters used in the TSM were those presented in Fig. 3(a) of the main text, and α as extracted from a semiclassical model [15] (marked in Fig. 3(b) using 80 % of their average peak intensity, 2.24×10^{14} W/cm^2) for each harmonic. In the TSM results presented in Fig. S12, only the short trajectory contributions were considered.

EUV ellipticity ε_{EUV} and tilt angle τ were obtained through the Stokes parameters, at the far-field spatial position at which each harmonic presents its maximum intensity. The satisfactory agreement between theoretical results and experimental measurements shown in Fig. 3 of the main text, together with the satisfactory agreement between TSM and quantum SFA results, allows us to corroborate the validity of the strong-field parameters (q_{eff}, α) retrieved from the experimental measurements in this work.

S7. Predominant role of the short vs. long quantum path in the non-collinear HHG geometry

In the non-collinear HHG geometry, so-called short quantum paths clearly dominate over long-quantum paths. We performed theoretical simulations within the SFA quantum model including propagation, and the TSM, to corroborate this effect. The parameters used in these simulations were those presented in preceding section S6.

First, in Fig. S13(a) we present the quantum SFA simulation results for the right-handed circularly polarized (RCP / left column) and left-handed circularly polarized (LCP /right column) projections of the far-field harmonic signal, in which the ellipticity of the drivers was $\varepsilon_{IR} = 0.7$. In the top panels we present the intensity spatial distribution, and in the other panels of Fig. S13(a) we present the time-frequency analysis of the radiation detected at three separate spatial positions for each

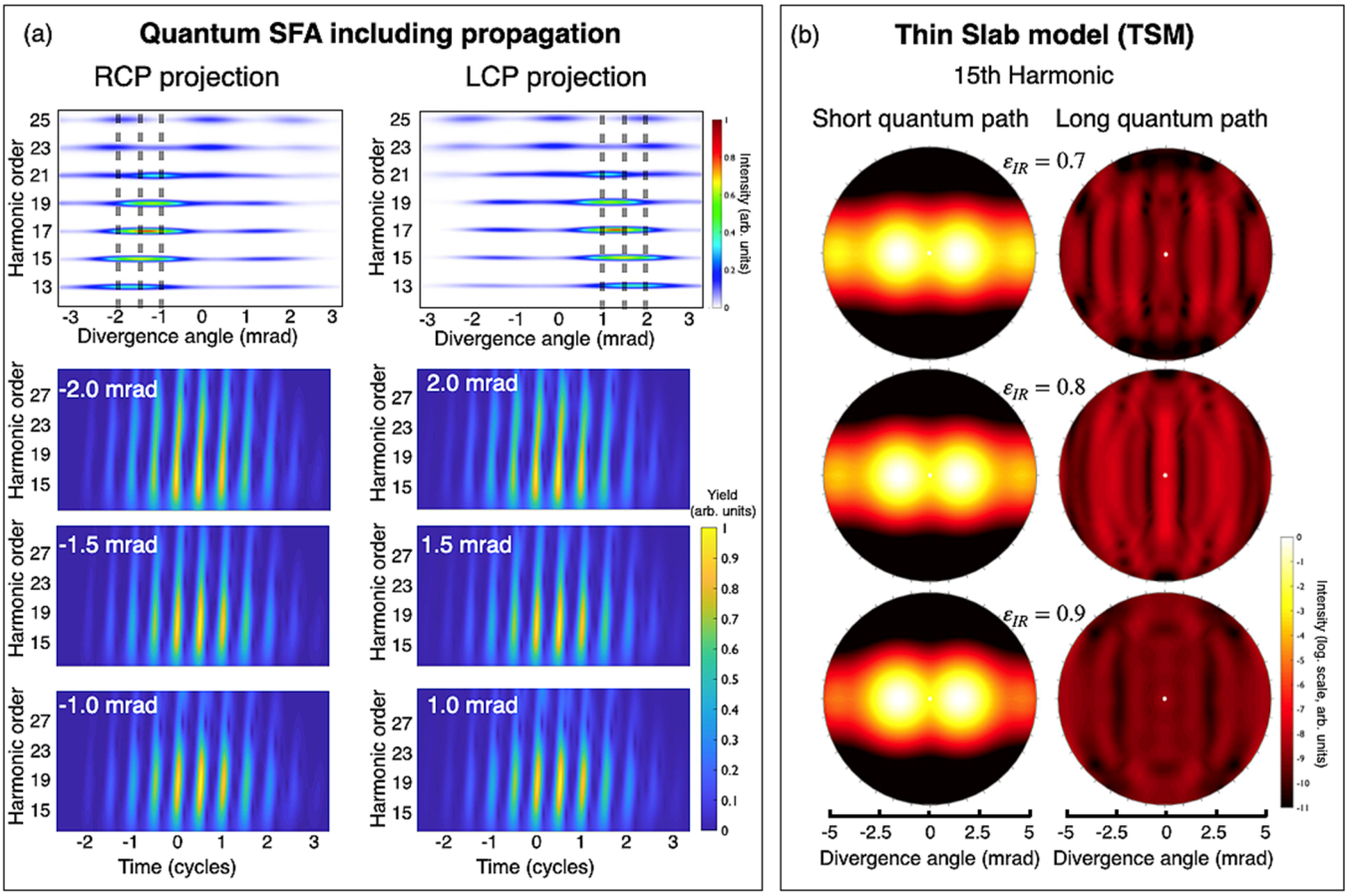

Fig. S13: Relevance of short quantum paths over long ones. (a) SFA quantum simulation results considering a driving field with $\varepsilon_{IR} = 0.7$, for RCP (left column) and LCP (right column) projections. The top panels show the far-field intensity distribution; the lower ones show the time-frequency analysis of the emission obtained at three divergence angles. The positive slope of the structures presented in all time-frequency analysis indicates the dominance of the short quantum paths. (b) TSM results of the far-field intensity distribution of harmonic 15 emitted through short (left column) and long (right column) quantum paths, and using a driving field with $\varepsilon_{IR} = 0.7$ (top row), $\varepsilon_{IR} = 0.8$ (middle row) and $\varepsilon_{IR} = 0.9$ (bottom row).

projection. The time-frequency analysis allowed us to observe at what time each harmonic was emitted. Short (long) trajectory contributions—which present a positive (negative) chirp—thus typically exhibited a structure with a positive (negative) slope in the time-frequency analysis. From an inspection of the six panels presented here, one can clearly see that the emission is dominated by short trajectory contributions.

Second, to corroborate this result, we show in Fig. S13(b) the TSM results of the distribution of spatial intensity of harmonic 15 when driven with $\varepsilon_{IR} = 0.7$ (top row), $\varepsilon_{IR} = 0.8$ (middle row) and $\varepsilon_{IR} = 0.9$ (bottom row), and when considering short trajectory contributions (left column, α = 3.529 deg./(10^{13}W/cm^2)) and long trajectory contributions (right column, α = 136.7 deg./(10^{13}W/cm^2)). The harmonic intensity is normalized to the same value in each row. Both shape and yield of the intensity distributions indicate that the short trajectories dominate over the long ones.

REFERENCES

1. T. Koide, T. Shidara, M. Yuri, N. Kandaka, K. Yamaguchi, and H. Fukutani, "Elliptical-polarization analyses of synchrotron radiation in the 5–80-eV region with a reflection polarimeter," *Nuclear Instruments and Methods in Physics Research Section A: Accelerators, Spectrometers, Detectors and Associated Equipment* **308**, 635–644 (1991).
2. P. Huang, C. Hernandez-Garcia, J. Huang, P. Huang, L. Rego, C. Lu, S. Yang, L. Plaja, A. H. Kung, et al., "Realization of Polarization Control in High-Order Harmonic Generation," *IEEE J. Select. Topics Quantum Electron.* **25**, 1–12 (2019).
3. M. Lewenstein, P. Salières, and A. L'Huillier, "Phase of the atomic polarization in high-order harmonic generation," *Phys. Rev. A* **52**, 4747–4754 (American Physical Society, 1995).
4. C. Corsi, A. Pirri, E. Sali, A. Tortora, and M. Bellini, "Direct Interferometric Measurement of the Atomic Dipole Phase in High-Order Harmonic Generation," *Phys. Rev. Lett.* **97**, 023901 (2006).
5. L. Quintard, V. Strelkov, J. Vabek, O. Hort, A. Dubrouil, D. Descamps, F. Burgy, C. Péjot, E. Mével, et al., "Optics-less focusing of XUV high-order harmonics," *Sci Adv* **5**, eaau7175 (2019).
6. C. Hernandez-Garcia, J. S. Román, L. Plaja, and A. Picón, "Quantum-path signatures in attosecond helical beams driven by optical vortices," *New J. Phys.* **17**, 093029 (2015).
7. L. Rego, J. S. Román, A. Picón, L. Plaja, and C. Hernández-García, "Nonperturbative Twist in the Generation of Extreme-Ultraviolet Vortex Beams," *Phys. Rev. Lett.* **117**, 163202EP– (2016).
8. P.-C. Huang, C. Hernández-García, J.-T. Huang, P.-Y. Huang, C.-H. Lu, L. Rego, D. D. Hickstein, J. L. Ellis, A. Jaron-Becker, et al., "Polarization control of isolated high-harmonic pulses," *Nature Photon* **12**, 349–354 (2018).
9. C. Hernández-García, J. A. Perez-Hernandez, J. Ramos, E. C. Jarque, L. Roso, and L. Plaja, "High-order harmonic propagation in gases within the discrete dipole approximation," *Phys. Rev. A* **82**, 033432 (2010).
10. L. V. Keldysh, "Ionization in the field of a strong electromagnetic wave," *Sov Phys JETP* **20**, 1307–1314 (1965).
11. F. H. M. Faisal, "Multiple absorption of laser photons by atoms," *J.*

Phys. B: At. Mol. Phys. **6**, L89–L92 (1973).
12. H. R. Reiss, “Effect of an intense electromagnetic field on a weakly bound system,” *Phys. Rev. A* **22**, 1786–1813 (1980).
13. C. Hernandez-Garcia, C. G. Durfee, D. D. Hickstein, T. Popmintchev, A. Meier, M. M. Murnane, H. C. Kapteyn, I. J. Sola, A. Jaron-Becker, et al., “Schemes for generation of isolated attosecond pulses of pure circular polarization,” *Phys. Rev. A* **93**, 043855 (2016).
14. D. D. Hickstein, F. J. Dollar, P. Grychtol, J. L. Ellis, R. Knut, C. Hernández-García, D. Zusin, C. Gentry, J. M. Shaw, et al., “Non-collinear generation of angularly isolated circularly polarized high harmonics,” *Nature Photon* **9**, 743–750 (2015).
15. M. B. Gaarde, J. L. Tate, and K. J. Schafer, “Macroscopic aspects of attosecond pulse generation,” *J. Phys. B: At. Mol. Opt. Phys.* **41**, 132001 (2016).